materials

MDPI

Article

Simulations on Monitoring and Evaluation of Plasticity-Driven Material Damage Based on Second Harmonic of S_0 Mode Lamb Waves in Metallic Plates

Xiaoqiang Sun [1], Xuyang Liu [1,*], Yaolu Liu [1], Ning Hu [1,2,*], Youxuan Zhao [1], Xiangyan Ding [1], Shiwei Qin [1], Jianyu Zhang [1], Jun Zhang [1], Feng Liu [3] and Shaoyun Fu [1]

[1] College of Aerospace Engineering, Chongqing University, Chongqing 400044, China; tiny_strong@sina.com (X.S.); liuyaolu@cqu.edu.cn (Y.L.); youxuan.zhao@cqu.edu.cn (Y.Z.); ddingxiangyan@yeah.net (X.D.); qsw123@163.com (S.Q.); jyzhang@cqu.edu.cn (J.Z.); mejzhang@cqu.edu.cn (J.Z.); syfu@cqu.edu.cn (S.F.)

[2] Key Disciplines Lab of Novel Micro-Nano Devices and System and International R&D Center of Micro-Nano Systems and New Materials Technology, Chongqing University, Chongqing 400044, China

[3] Department of Engineering Mechanics, College of Mechanical and Vehicle Engineering, Hunan University, Changsha 410082, China; liufengeaddr@126.com

* Correspondence: liuxuyang@cqu.edu.cn (X.L.); ninghu@cqu.edu.cn (N.H.); Tel.: +86-023-6510-2527 (N.H.)

Received: 13 May 2017; Accepted: 12 July 2017; Published: 19 July 2017

Abstract: In this study, a numerical approach—the discontinuous Meshless Local Petrov-Galerkin-Eshelby Method (MLPGEM)—was adopted to simulate and measure material plasticity in an Al 7075-T651 plate. The plate was modeled in two dimensions by assemblies of small particles that interact with each other through bonding stiffness. The material plasticity of the model loaded to produce different levels of strain is evaluated with the Lamb waves of S_0 mode. A tone burst at the center frequency of 200 kHz was used as excitation. Second-order nonlinear wave was extracted from the spectrogram of a signal receiving point. Tensile-driven plastic deformation and cumulative second harmonic generation of S_0 mode were observed in the simulation. Simulated measurement of the acoustic nonlinearity increased monotonically with the level of tensile-driven plastic strain captured by MLPGEM, whereas achieving this state by other numerical methods is comparatively more difficult. This result indicates that the second harmonics of S_0 mode can be employed to monitor and evaluate the material or structural early-stage damage induced by plasticity.

Keywords: lamb waves; material plasticity; second-order nonlinear wave; monitoring; evaluation

1. Introduction

An effective and reliable inspection technique for continuous monitoring and evaluation of early-stage nonlinearities in materials is necessary for engineering parts. Among all kinds of nondestructive methods studied for efficient damage detection and evaluation, the ultrasonic method is most useful and has been widely exploited for many decades [1–4]. Traditional ultrasonic inspection and monitoring methods are usually anchored on linear theory, and the characterization parameters are velocity attenuation, transmission, and reflection coefficients of the ultrasonic wave. However, conventional linear ultrasonic evaluation and monitoring methods are not sensitive to early stage micro-damage or micro-plastic deformation [4], and the smallest crack that current linear ultrasonic based approaches can monitor or evaluate is only approximately 1 mm [5]. This drawback limits their applications and does not allow early preventive actions [5–7].

When a high-intensity ultrasonic wave passes through a nonlinear medium, the waveform may be distorted [8]. It is well-known that a linear solid medium may become a nonlinear one gradually in the process of fatigue damage [9], radiation damage [10], hardening [11], and thermal aging [12]

as the microstructural features are occupied by micro-voids, multi-poles, and micro-cracks [13], dislocation [14–16], persistent slip bands [17], and precipitation characteristics [18]. When a finite amplitude monochromatic sinusoidal ultrasonic wave interrogates a nonlinear solid, the initial waveform distorts and higher-order harmonic waves are generated. Overcoming the limitations of the linear ultrasonic method, the nonlinear ultrasonic technique measures higher harmonics generated by material intrinsic nonlinearity, and this technique has undergone rapid development in recent years. In most experiments or theoretical studies, only bulk waves are used, and a useful acoustic nonlinearity parameter presenting material nonlinearity is established by theoretical models [8,19,20]. However, bulk waves propagate with great energy loss and are not efficient in a large-scale inspection approach.

Guided waves, such as Lamb waves, combine large-scale monitoring or inspection ranges and the sensitivity of nonlinear parameters, which could be used for long-range monitoring or inspection to interrogate large shell- and plate-like structures. However, the monitoring or inspection techniques based on nonlinear Lamb waves might not be highly accurate because of their depressiveness and multiple modes. About the conditions to generate accumulative higher-order harmonic waves, corresponding theoretical studies may not be sufficiently clear and consistent because of the mathematical complexity of the problem [21–27]. To date, all theoretical studies agree that phase-velocity matching and non-zero power flux input from a primary mode to second harmonics are at least two necessary conditions for cumulative second harmonic generation. Mode pairs that satisfy these two conditions, such as S_1–S_2, S_2–S_4, and A_2–S_4 have been used in experimental studies. These nonlinear Lamb wave–based experiments have effectively characterized tensile plasticity driven damage [28], material nonlinearity [29], thermal fatigue [30], and fatigue damage [31], and have monitored the stress and load levels in strands [32]. However, using those higher-order mode as primary Lamb wave mode has some limitations in application [7]. First, in real applications, as the excitation signal is normally a tone burst with a finite bandwidth, strict phase velocity matching only exists at the center frequency of the whole bandwidth. Second, excited center frequency of the primary mode may not be exactly equal to the true phase-velocity-matching frequency. Third, mode pairs are isolated and quite limited in number. Fourth, exciting a single primary mode of the mode pairs as desired is extremely difficult in practice and some unwanted modes would be generated simultaneously, making the received signal quite difficult to be processed and interpreted. Finally, time-frequency analysis is needed to process the received complicated signals in which some unwanted Lamb modes overlap with the desired primary and secondary modes [7]. S_0 mode Lamb wave could solve these limitations and this has been confirmed by many researchers. For instance, Wan et al. [7] used the cumulative effect of the second harmonic generated from S_0 mode Lamb waves for the detection of microstructural changes [7]. Zuo et al. [33] calculated nonlinear harmonic of low frequency S_0 wave for a 1.0 mm thick aluminum plate using the Murnaghan model, which is equivalent to the Landau–Lifshitz nonlinear hyper elastic constitutive model. Chillara and Lissenden [34] used the same Murnaghan model for an aluminum plate and found that the second harmonic can propagate independently to the primary mode and the group velocity matching is not necessary for higher harmonic generation by numerical study of S_0 mode Lamb waves. By considering the effects of the second- and third-order elastic constants of isotropic media, Matsuda and Biwa [35] revealed that the frequency for which the second harmonic Lamb mode reaches maximum is close but not equal to the phase speed-matching frequency in a precise sense through theory and Finite-Difference Time-Domain method for S_0 Lamb mode waves. Shan et al. [36] demonstrated that the nonlinear effects of the bonding layers in a typical PZT-actuated structural health monitoring system by using S_0 mode Lamb waves. For micro-cracks, there are also some works using S_0or A_0Lamb waves [37–44]. However, there has been no work using the S_0 mode Lamb wave to characterize tensile plasticity-driven damage.

It is well known that numerical exploration is attractive in ultrasonic nondestructive testing (NDT) to verify theoretical and experimental results and to find some new phenomena difficultly tackled by theory or experiment. The advantages of this method include ideal center frequency and single desired primary mode excitation [7], reduced cost, celerity, and simplicity. For instance, nonlinearities induced

by buried micro-breathing cracks [32,37–44], material and geometry [45], and fatigue damage [46] are simulated through finite element method (FEM). The aforementioned simulations investigate on cumulative second-harmonic generation. In general, FEM, finite volume method, finite difference method, and boundary element method are suitable for simulating dynamic behaviors of continuum medium. However, special additional treatments, such as intensive remeshing to tackle mesh distortion caused by finite deformation and contact judgment, have to be considered in the calculation, where damage or fracture appears, simulating the entire failure procedure is difficult [47]. Under tensile loading, the plasticity-driven material damage and its evolution process is a problem that is difficult to simulate by commercial software such as ABAQUS or ANSYS. To ensure improved understanding of plasticity-driven cumulative second-harmonic generation, an alternative simulation method that could solve the problem is the discontinuous Meshless Local Petrov-Galerkin-Eshelby Method (MLPGEM), which is similar to the Discrete Element Method. It is very efficient for solving finite deformation nonlinear problems. For instance, it requires no explicit mesh in computation and therefore avoid mesh distortion difficulties and subsequent remeshing effort of traditional FEM in finite deformation analysis. Therefore, it should be a powerful tool to simulate the wave propagation in a largely deformed medium with the plasticity-driven material damage and its evolution process under tensile loading.

In this study, an MLPGEM module released by commercial software LS-DYNA is employed directly to deal with the above problem. The theory of MLPGEM and material plasticity is briefly explained as a foundation for simulating nonlinear Lamb waves. Unlike most previous works using those higher-order mode as primary Lamb wave mode [13,28–32], e.g., S_1, S_2, A_2, etc., we focus on the case of S_0 primary mode because of its remarkable merits [7] and investigate its second-harmonic generation. S_0 Lamb wave with tone-burst cycles of 10 at the center frequency of 200 kHz has been used as a primary mode in the simulation. As shown in Figure 1, the condition of phase-velocity matching [21–25,31] can be satisfied approximately when considering S_0 (400 kHz) as the second harmonic of this primary mode. The detailed descriptions of the numerical model as well as signal excitation and processing are presented. The results for the simulated material plasticity versus tensile strain and acoustic nonlinearity parameter corresponding to the different plasticity levels are provided and discussed. The results show that S_0 Lamb wave and its corresponding second harmonic can be effectively employed to monitor and evaluate the plasticity driven early stage material damage.

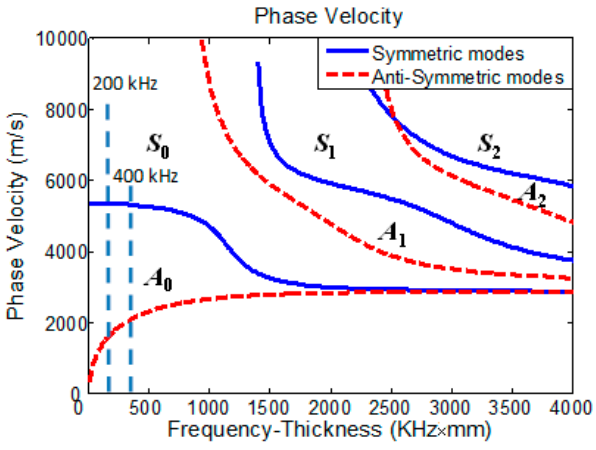

Figure 1. Dispersion curves of Lamb waves in an aluminum plate: phase velocity.

2. Material Nonlinearity and Its Measurement

Theoretical models for longitudinal waves in one-dimensional medium [46] and Lamb waves in isotropic, homogeneous, and nonlinear elastic infinite plate [22,27] show that the acoustic nonlinearity parameter of a material, i.e., β can be defined as,

$$\beta = \frac{8}{xk^2}\left(\frac{A_2}{A_1^2}\right) \tag{1}$$

where k is wavenumber, x is wave propagation distance, A_1 is magnitude of the primary wave mode at ω, and A_2 is second harmonic wave mode at 2ω. The amplitude ratio A_2/A_1^2 is a measure of the nonlinearity parameter β and is widely used in experiments and simulations [38,45,48–51]. A monotonic increase between β and the accumulated plasticity of some metals was confirmed for bulk waves [17,52] and Lamb waves with S_1–S_2 pair [28]. Therefore, the tensile-plasticity-driven material damage might be characterized by directly measuring A_2/A_1^2.

3. Theory and Model of MLPGEM

3.1. Theory

MLPGEM combines the Meshless Local Petrov-Galerkin (MLPG) Methods of Atluri and the energy conservation laws of Noether and Eshelby [53]. MLPG is a truly meshless method that involves both non-element interpolation and non-element integration [54]. MLPG may alleviate problems such as element distortion, locking, remeshing during large deformation process. With the help of the "energy-momentum tensor" given by Eshelby, Han and Atluri solved the singular integrals appearing in the local boundary integral equation and proposed a numerical method called MLPGEM [53]. This method is simply described as follows: a body is assembled by spheres (in 3-D or circles in 2-D) centered at each meshless node. The moving least squares (MLS) approximation over a number of nodes within the domain of influence is used to construct the trial functions. Trial functions is based on the fictitious nodal value of the undeformed configuration. The test functions for configurational changes of the deformed configuration are also based on meshless nodes. While the local sub-domain is defined as the support of the test function on which the integration is carried out, the domain of influence is defined as a region where the weight function of the node inside of it does not vanish in the local sub-domain of the current node. In other words, the domain of influence contains all the nodes that have non-zero coupling with the current nodal values in the stiffness matrix. In Figure 2a, the sphere surrounding node I represents the local sub-domain where the integration is carried out. The spheres surrounding node J, K, L, M ... represent the supporting domain of weight functions of nodes, whose weight functions do not vanish in the local sub-domain. The volume surrounded by dashed curve represents the domain of influence of node I. In general, the size of the domain of influence has to be large enough in order to ensure continuity. Piecewise-linear predictor solutions are generated based on the local weak-forms of the Noether/Eshelby energy conservation laws for the Lagrangian unsymmetric Eshelby stress tensor in the undeformed configuration. Corrector solutions are generated based on Newton-Raphson (or Jacobian-inversion-free iterations) using the local weak-forms of the Noether/Eshelby energy conservation laws in the current configuration, for a newly introduced Eulerean symmetric stress tensor (which is the counter part of the Lagrangian unsymmetric Eshelby stress tensor) in the current configuration.

We consider the finite deformation of a solid, wherein a material particle initially at $\mathbf{X}$, moves to a location $\mathbf{x}$. We use a fixed Cartesian coordinate system with base vectors $\mathbf{e}_i$, such that,

$$\mathbf{X} = X_I \mathbf{e}_i \tag{2}$$

$$\mathbf{x} = x_i \mathbf{e}_i \tag{3}$$

The displacement of the material particle is,

$$\mathbf{u}(\mathbf{X}) = \mathbf{x}(\mathbf{X}) - \mathbf{x} \text{ or } u_i = (x_i - X_I)\mathbf{e}_i \tag{4}$$

The deformation gradient tensor is defined as,

$$\mathbf{F}\left[F_{iJ}=\frac{\partial x_i}{\partial X_J}\equiv x_{i,J}=u_{i,J}+\delta_{iJ}\right] \tag{5}$$

There are infinitely many possible definitions of a stress-tensor in a finitely deformed solid. Among them, the more commonly used ones are: the Cauchy stress tensor σ; the first Piola-Kirchhoff stress tensor $\mathbf{P}$; and the second Piola-Kirchhoff stress $\mathbf{S}$, which are related to each other, thus,

$$\mathbf{P}=J\mathbf{F}^{-1}\boldsymbol{\sigma}=\mathbf{S}\cdot\mathbf{F}^{t};\mathbf{S}=J\mathbf{F}^{-1}\cdot\boldsymbol{\sigma}\cdot\mathbf{F}^{-t}=\mathbf{P}\cdot\mathbf{F}^{-t}[J=\|\mathbf{F}\|] \tag{6}$$

Considering a general anisotropic solid, with the strain energy per unit initial volume being denoted as W, the constitutive relation for $\mathbf{P}$ may be written as,

$$\mathbf{P}=\frac{\partial W}{\partial \mathbf{F}^{t}} \tag{7}$$

The equations of Linear Momentum Balance (LMB) and Angular Momentum Balance (AMB) can be written equivalently in terms of σ, $\mathbf{P}$, and $\mathbf{S}$, as,

$$\begin{array}{l}\sigma_{ij,i}+\rho f_j=0;(LMB);\boldsymbol{\sigma}=\boldsymbol{\sigma}^{t}(AMB)\\ P_{Ij,I}+\rho_0 f_j=0;(LMB);\mathbf{F}\cdot\mathbf{P}=\mathbf{P}^{t}\cdot\mathbf{F}^{t}(AMB)\\ \left(S_{IK}F_{jK}\right)_{,I}+\rho_0 f_j=0;(LMB);\mathbf{S}=\mathbf{S}^{t}(AMB)\end{array} \tag{8}$$

The Eshelby stress tensor is defined, for finite deformations, as,

$$\mathbf{T}=W\mathbf{I}-\mathbf{P}\cdot\mathbf{F}=W\mathbf{I}-\mathbf{S}\cdot\mathbf{F}^{\mathbf{t}}\cdot\mathbf{F}=W\mathbf{I}-\mathbf{S}\cdot\mathbf{C} \tag{9}$$

The strong form balance laws for the Eshelby stress tensor $\mathbf{T}$ is given as,

$$T_{IJ,I}+\rho_0 b_J=-(P_{Ik,I}+\rho_0 f_k)F_{kJ}=0,(LMB),\mathbf{C}\cdot\mathbf{T}=\mathbf{T}^{t}\cdot\mathbf{C},(AMB) \tag{10}$$

where, by definition,

$$b_J\equiv\frac{1}{\rho_0}W_{,J}\big|_{\exp.}+f_k F_{kJ} \tag{11}$$

We refer the solution variables (displacements, deformation gradient, and stresses) in the state $C^{(N+1)}$to the configuration of the body in the immediately preceding state, denoted as $C^{(N)}$, which is presumed to be known, including the variables in $C^{(N)}$, such as $\mathbf{u}$, $\mathbf{F}$, σ, and $\mathbf{T}$, with the initial configuration $C^{(0)}$being the reference configuration, as shown in Figure 2b. Let $\tilde{\mathbf{v}}(\mathrm{X})$ be the configurational changes of the initial configuration which are the trial functions in the present MLPGEM, and let the corresponding changes to the displacements in $C^{(N)}$ as given in equation$\Delta\mathbf{u}=\mathbf{F}\cdot\tilde{\mathbf{v}}(\mathrm{X})$. One may have the spatial tangential material stiffness for $\Delta\mathbf{S}_{IJ}$in the configuration $C^{(N)}$, derived as,

$$\Delta\mathbf{S}_{IJ}=\frac{1}{2}\frac{\partial^2 W}{\partial E_{IJ}\partial E_{MN}}F_{kM}F_{lN}[F_{\mathrm{k}K}F_{Ll}^{-1}+F_{Lk}^{-1}F_{lK}]\Delta L_{KL}^{*}\equiv C_{IJKL}^{*}\Delta K_{KL}^{*} \tag{12}$$

The local weak-forms of the energy conservation laws can be derived as,

$$\begin{array}{l}\left\{\int_{\partial\Omega_N^{(I)}}\mathrm{n}_i c_{ijKL}^{\tan\mathrm{gent}}\Delta K_{KL}^{*}\delta x_j dS-\int_{\Omega_N^{(I)}}c_{ijKL}^{\tan\mathrm{gent}}\Delta K_{KL}^{*}\delta x_{j,i}d\Omega\right\}+\left\{\int_{\partial\Omega_N^{(I)}}\rho_N\Delta f_j\delta x_j d\Omega\right\}\\ +\left\{\int_{\partial\Omega_N^{(I)}}\mathrm{n}_i\sigma_{ij}^{(N)}\delta x_j dS-\int_{\Omega_N^{(I)}}\sigma_{ij}^{(N)}\delta x_{j,i}d\Omega+\int_{\Omega_N^{(I)}}\rho_N f_j^{N}\delta x_j d\Omega\right\}=0,\\ \mathrm{c}_{ijKL}^{*}\equiv\frac{1}{J^{(N)}}(F_0^N)_{iM}\cdot C_{MNKL}^{*}\cdot(F_0^N)_{jN}\text{ and }c_{ijKL}^{\tan\mathrm{gent}}=c_{ijKL}^{*}+\sigma_{IM}^{(N)}F_{jK}F_{KL}^{-1}\\ \text{and }\boldsymbol{\sigma}^{(N)}=\frac{1}{J^{(N)}}(\mathbf{F}_0^N)\cdot(\mathbf{S}_0^N)\cdot(\mathbf{F}_0^N)^{t}.\end{array} \tag{13a}$$

With a constant test function $\delta \mathbf{x}$ over each local sub-domain, the domain integrals vanish and the local weak-forms of the energy conservation laws may be further simplified as,

$$\left\{ \int_{\Omega_N^{(IJ)}} \frac{1}{2}[(c_{ijKL}^{\text{tangent}} \Delta L_{KL}^*)^{(J)} + ((c_{ijKL}^{\text{tangent}} \Delta L_{KL}^*)^{(I)}](\delta x_j^J - \delta x_j^I) dS \right\} = \left\{ \begin{array}{c} \int_{\partial\Omega_N^{(I)}} \rho_N \Delta f_j \\ \delta x_j d\Omega \end{array} \right\} + \left\{ \int_{\Omega_N^{(I)}} \rho_N f_j^N \delta x_j d\Omega - \int_{\partial\Omega_N^{(IJ)}} \frac{1}{2}[(\sigma_{ij}^{(N)})^{(J)} + (\sigma_{ij}^{(N)})^{(I)}](\delta x_j^J - \delta x_j^I) dS \right\} \quad (13b)$$

Once the trial functions $\tilde{\mathbf{v}}(\mathrm{X})$ (configurational changes in the initial configuration) are solved through Equation (13), corresponding to either the unbalanced force or to the incremental loading, the corresponding displacements can be obtained through $\Delta \mathbf{u} = \mathbf{F} \cdot \tilde{\mathbf{v}}(\mathrm{X})$. It is clear that Equation (13) can be applied in both Total Lagrangian formulation or an Updated Lagrangian formulation by setting the displacements $\mathbf{u}(\mathbf{X})$ of the preceding solution accordingly. In Equation (13b), $c_{ijKL}^{\text{tangent}}$ is the quantity to reflect the current material properties, e.g., elastic or plastic behavior at different loading stages in the analysis, which can be understood as the nonlinear stiffness connecting nodes or spheres in Figure 2a. One may see further details in the references [53–55].

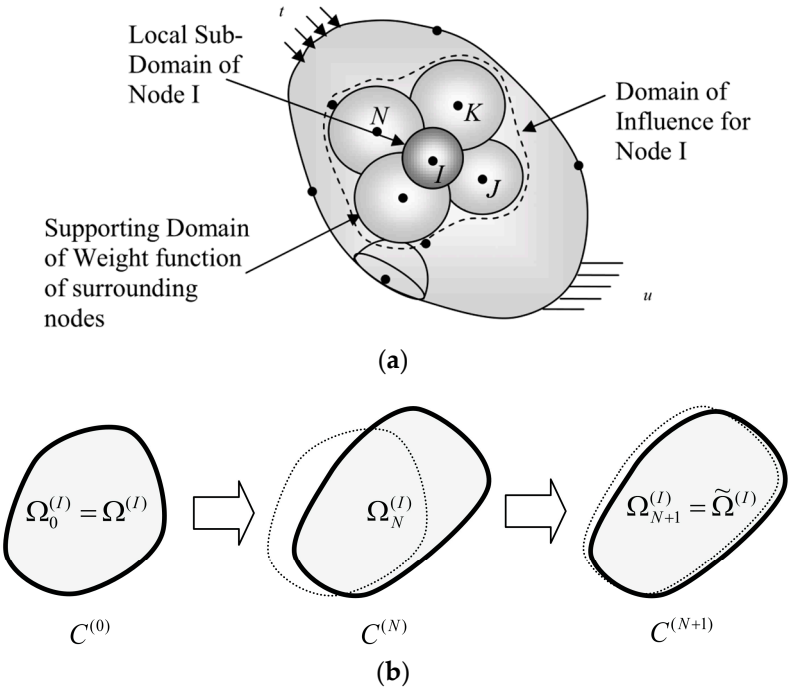

Figure 2. Description of MLPGEM: (**a**) trial and test domain; (**b**) three configurations during a finite deformation.

3.2. Model

Figure 3 shows the MLPGEM model (Livermore Software Technology CORP., California, CA, USA). The Lamb waves of S_0 mode propagating in an aluminum plate is symmetrical in the y-axis direction. For simplicity, the plate with thickness 1 mm could be modeled in two dimensions by assemblies of small spheres. The model should be long enough (2.0 m) to ensure that the received signals are not affected by boundary reflections.

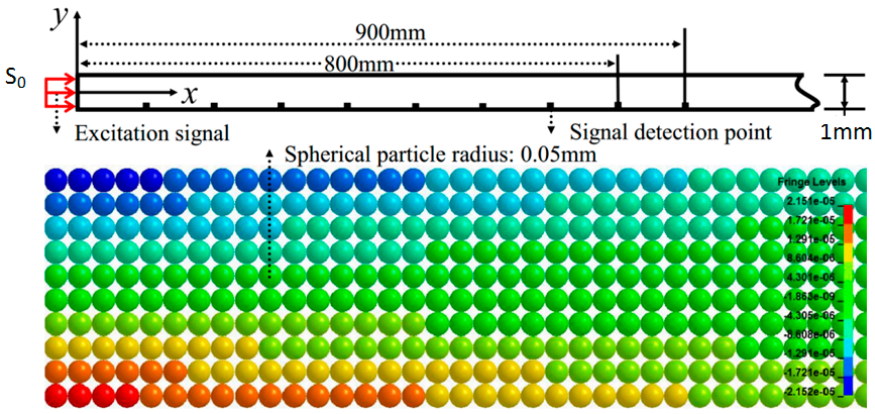

Figure 3. Meshless Local Petrov-Galerkin-Eshelby Method (MLPGEM) model.

A loading process can be described as: a tensile load is slowly applied on the plate which makes the plate be deformed into a state needed, and the deformed plate is hold to keep this deformation. Lamb waves of S_0 mode in terms of a designed function are then generated with the line source signal excitation acting on the left side of the present plate. The loading function of the above process can be described as,

$$x(t) = \begin{cases} \frac{l}{2}(\cos(\frac{2\pi}{T}t) - 1) & t \in [0, \frac{T}{2}) \\ -l & t \in [\frac{T}{2}, t_1) \\ \frac{A}{2}\sin(2\pi f t)(1 - \cos(2\pi\frac{f}{N}t)) - l & t \in [t_1, t_2) \\ -l & t \in [t_2, t_e] \end{cases} \quad (14)$$

where l is the tensile length in mm, T is the period of tensile function in ms, f is the central frequency in kHz, N (=10) is the number of sinusoidal cycles in a wave pulse, $\frac{T}{2}$ is the end time of the tensile process, A (=0.01 mm) is the amplitude of tone burst, t_1 is the end time of the holding process, t_2 is the end time of the loading (Hamming windowed tone-burst consisting of 10 cycles at the center frequency 200 kHz), and t_e is the end time of the simulation.

When l is equal to 30 mm—for example, the loading function is shown in Figure 4—the plate is stretched by 30 mm with a strain of 0.015. Seven different ls (i.e., 0 mm, 5 mm, 10 mm, 15 mm, 20 mm, 25 mm, and 30 mm) were loaded in our model. A large l needs a large T and t_1. In our simulation, nine signal receiving points are considered with a distance from 100 mm to 900 mm with an interval of 100 mm from the left of the model, where the excitation signal actuated, as illustrated in Figure 3.

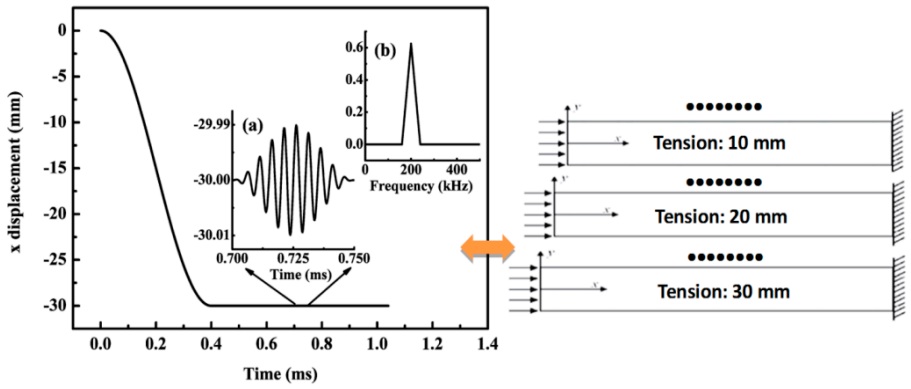

Figure 4. Actuating function of excitation signal with stretching length l = 30 mm and T = 0.8 ms: (**a**) time domain and (**b**) frequency domain.

The MLPGEM module of LS-DYNA with the Newton-Raphson iterations method is used in this study. For fundamental signal 200 kHz and higher harmonics 400 kHz, a mesh size of 0.1 mm (particle radius 0.05 mm) and a time step of 0.02 μs are suitable and enough to ensure accuracy [56,57]. For undamaged Al 7075-T651 plate, piecewise linear plasticity with failure was chosen as the material model, and the stress–strain constitutive relationship is shown in Figure 5. In the present work, the plasticity of aluminum 7075-T651 was represented by a nonlinear stress-strain curve. The practical experimental tensile stress-strain curve was used. We explain our modelling as follows: the nonlinear constitutive law is a two-stage one, i.e., the linear elastic stage and nonlinear plastic stage after yielding as shown in Figure 5. The Mises yield surface is used to judge isotropic yielding. It is defined by giving the value of the uniaxial yield stress as a function of uniaxial equivalent plastic strain. Below the yielding strength, the material behavior was modeled in a linear way as shown in Figure 5. After the yielding, the material plastic behavior was modeled in a piecewise linear pattern using some discrete points as shown in Figure 5. This plasticity should be considered to be caused by dislocations in the material, which is different to hyper-elasticity. Therefore, we employ a classical phenomenological plastic model here. Our method, unlike the theoretical way to deal with material nonlinearity, does not use higher-order expansion of the constitutive relation between the applied stress and resulting strain.

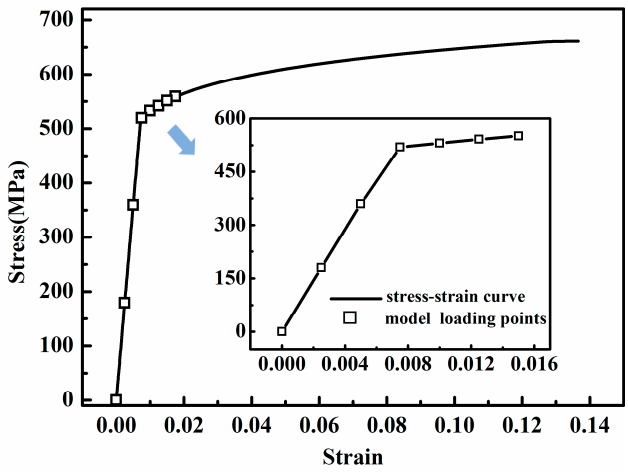

Figure 5. Stress–strain curve of Al 7075-T651 plate with maximum strains loaded for the seven models.

In fact, a material table was defined relating the different strain-levels to the stress levels. The seven representative tensile stresses with the corresponding maximum strains at different levels represented by a symbol of square are also plotted in Figure 5. The first four points simulate the elastic zone and they form a straight line. The nonlinear stress-strain zone is approximated using the piecewise linear model with more discrete points. The material properties are shown in Table 1.

Table 1. Material properties of Al 7075-T651.

Material	ρ(g/mm^3)	E (MPa)	Poisson's Ratio	Yield Stress (MPa)
Al 7075-T651	2.7957×10^{-3}	7.1705×10^{4}	0.33	517.84

4. Simulation Results and Discussion

4.1. Effectiveness Validation of MLPGEM

For an unloaded plate, Figures 6a,b and 7 indicate that the through thickness profile for displacement in y-axis direction is antisymmetric and for displacement in x-axis direction is symmetric. Note that h denotes the distance from the bottom surface of the plate and all curves in Figure 7 are overlapped.

Thus, a pure symmetric mode Lamb wave (S_0) with center frequency of 200 kHz is excited in our MLPGEM model. To verify the validity of our model further, group velocity verification for Lamb waves of symmetric and antisymmetric modes at center frequency of 100 kHz and 200 kHz are tested. Note that for A_0 mode, the shear stress was applied at the left end of the plate in Figure 2. The velocity results shown in Table 2 agree with the theoretical results within the allowable error range. Based on the preceding research, the validity of our MLPGEM model is verified.

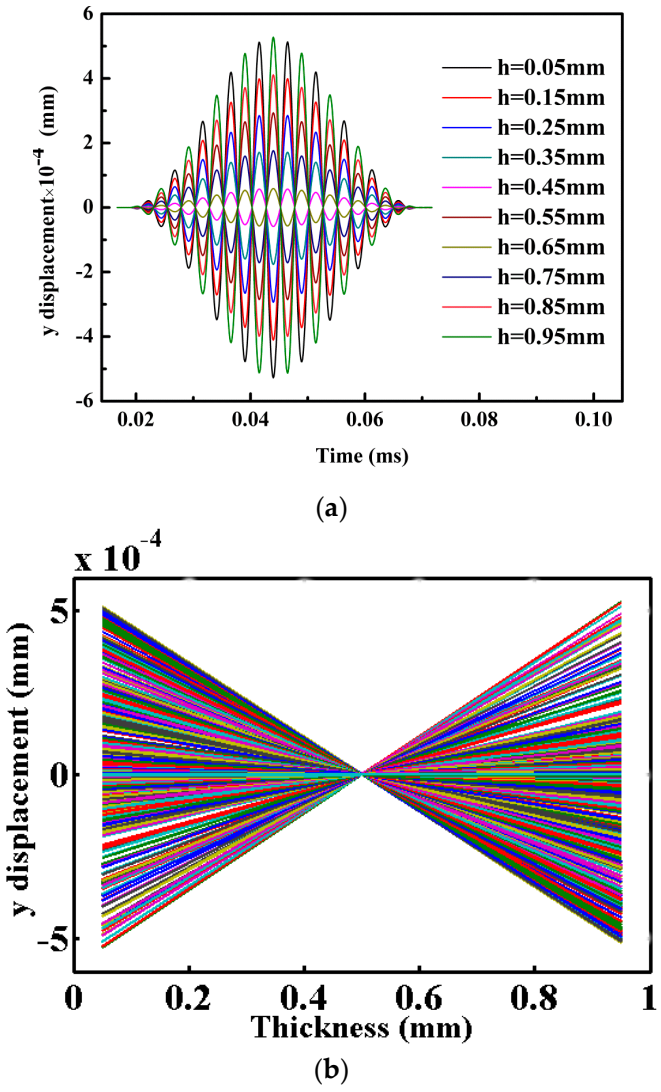

Figure 6. (**a**) Displacement in *y*-axis direction at different locations through-thickness direction with the same *x* coordinate (=100 mm); (**b**) S_0 mode at 200 kHz—through thickness profiles for *y* displacement at *x* coordinate (=100 mm) for various times *t* = 0.02–0.07 ms.

Table 2. Group velocity verification for symmetric (S_0) and antisymmetric (A_0) mode Lamb waves at center frequencies of 100 kHz and 200 kHz.

Mode Type and Frequency (kHz)	Theoretical Velocity (m/s)	Simulation Velocity (m/s)	Error (%)
S_0 (100 kHz)	5444	5263	3.32
S_0 (200 kHz)	5437	5235	3.72
A_0 (100 kHz)	1748	1707	2.35
A_0 (200 kHz)	2283	2252	1.36

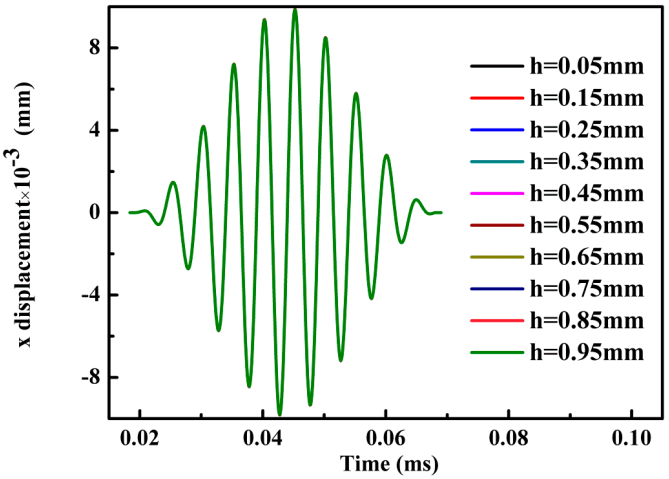

Figure 7. Displacement in x-axis direction at different locations through-thickness direction with the same x coordinate (=100 mm).

4.2. Simulation Results and Discussion

Figure 8a (time domain) and Figure 8b (frequency domain) show the received signal when Lamb waves propagate through 300 mm. As indicated in Figure 8b, second harmonics are generated at an amplitude ratio of 0.3280, denoted by A_2/A_1^2. For each l (0 mm, 5 mm, 10 mm, 15 mm, 20 mm, 25 mm, and 30 mm) in the actuating function described in Equation (14), we computed the amplitude ratios of the received signals from the nine signal receiving points, and then we plotted the results in Figure 9 to compare and analyze for convenience. In the signal processing using Fast Fourier Transformation (FFT), the window length of a rectangular function was adjusted continuously (but valid signals were not cut off) until the center frequency of the primary fundamental wave was 200 kHz. We could then obtain comparatively more accurate and consistent data.

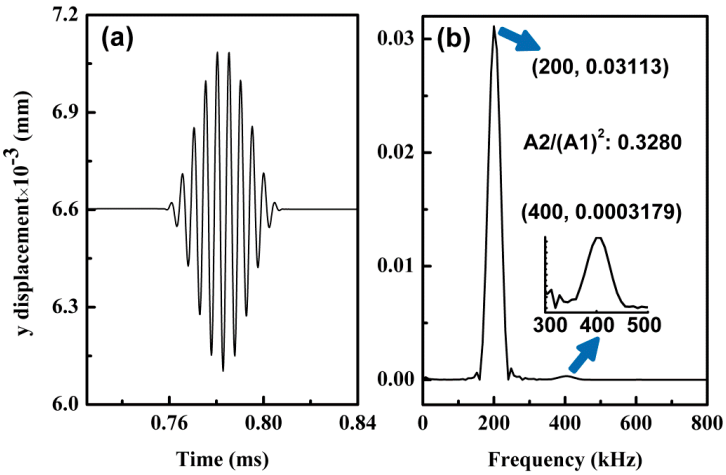

Figure 8. Signal received at propagation distance of 300 mm for S_0 at 200 kHz with maximum strain 0.015 (tension 30 mm): (**a**) time domain and (**b**) frequency domain; amplitude ratio is 0.3280.

Figure 9 shows the amplitude ratio, i.e., A_2/A_1^2, which is a linear function of propagation distance. The lines can be categorized into two groups. The first group includes tensile strains 0.01 (l = 20 mm), 0.0125 (l = 25 mm), and 0.015 (l = 30 mm, note that the yield strain is 0.0072) with larger slopes. The second group consists of tensile strains 0, 0.0025 (l = 5 mm), 0.005 (l = 10 mm), and 0.0075 (l = 15 mm) with smaller slopes. The slopes of the lines in each group are too close to distinguish. In every group at

the same propagation distance, the amplitude ratio is slightly larger when the stretching deformation is larger. Thus, the greater the tension, i.e., plasticity extent, is, the larger is the amplitude ratio (acoustic nonlinearity). When the tensile strain exceeds the yield stain to an extent, a remarkable increase of the amplitude ratio occurs suddenly as concluded more clearly in Figure 10.

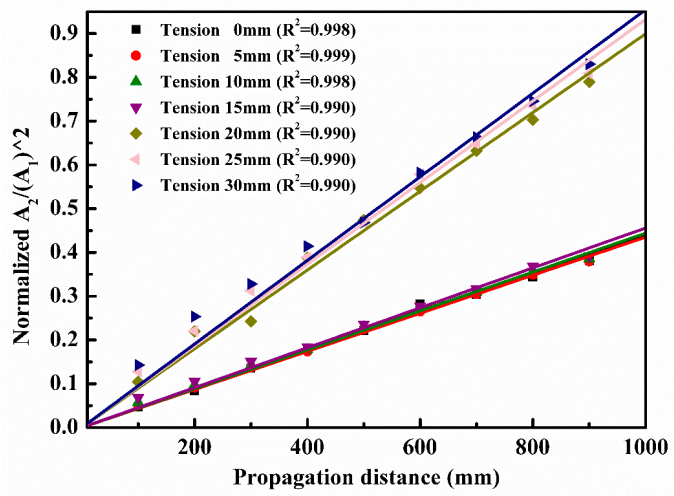

Figure 9. Amplitude ratio A_2/A_1^2, a measure of the nonlinearity parameter β, plotted as a function of propagation distance for the seven models (linearly fitted lines passing through the origin).

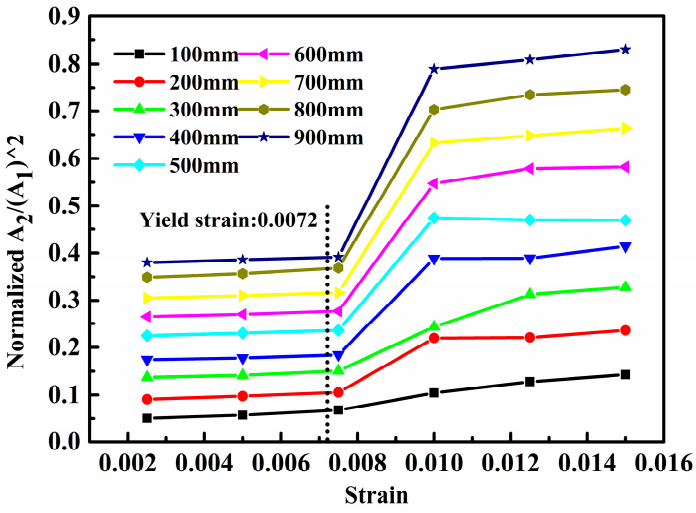

Figure 10. Normalized acoustic nonlinearity versus strain with the model.

Figure 10 shows a plot of A_2/A_1^2 versus the strain of the Lamb wave. The signal receiving points range from 100 mm to 900 mm with an interval of 100 mm. Note that when we used different amplitudes A of excitation signals in Equation (2) (e.g., 0.001 mm and 0.1 mm) or different frequencies (e.g., 100 kHz and 300 kHz), the change tendencies of A_2/A_1^2 in Figures 9 and 10 were similar. Figure 10 shows that the amplitude ratio at different propagation distances exhibit the similar variation pattern. At the yield strain, i.e., 0.0072, A_2/A_1^2 increases remarkably. Compared with those inelastic stage, A_2/A_1^2 in plasticity deformation have an approximate 200% increase at around 0.01 tensile strain. For further higher plastic strain levels, both Figures 9 and 10 show that the amplitude ratio increases only slightly. This feature of increasing trend in A_2/A_1^2 of is similar to what the theoretical models [17,52,58] for bulk waves predict essentially and has been verified by experiments when using those higher-order modes of Lamb waves as primary mode, e.g., S_1 or S_2 [28]. The amplitude ratio increases remarkably

at the happening of plasticity and this increase becomes much weaker with subsequent accumulated plasticity. Thus, Lamb waves of S_0 mode can be used to evaluate plasticity driven material damage, or at least is capable of characterizing the occurring of plasticity.

In the simulation process of tension, geometrical discontinuous defects (such as cracks, voids, dislocations, and impurity) were not modelled. However, A_2/A_1^2 caused by these defects is completely reflected in the stress–strain curve in the present simulations, i.e., material softening.

Therefore, the present model is reasonable for simulating material plasticity. Moreover, the above results imply that A_2/A_1^2 based on S_0 mode can be used to characterize plasticity-driven material damage, or at least, to monitor the occurring of plasticity. After entering into the plasticity, with the further increase of tensile strain, there are only slight increases in A_2/A_1^2, although this A_2/A_1^2 is around two times higher thanthat of material in elastic deformation. Whether A_2/A_1^2 can be used to accurately characterize the plasticity extent or not still needs more extensive explorations.

The above simulation results are also verified by some experiments reported by others indirectly. For example, C. Pruell et al. [28] develops an experimental method for evaluating damage due to plastic deformation in a metal plate using nonlinear-guided waves. The material nonlinearities of aluminum specimens loaded to produce different levels of plastic strain are measured with Lamb waves. A pair of wedge transducers is used to generate and detect the fundamental (S_1) and second harmonic (S_2) Lamb waves. The weak amplitude of the second harmonic wave is extracted from the spectrogram of a received signal. The measured acoustic nonlinearity increases monotonically with the level of plastic strain, which is similar to our simulations. After the plasticity stage, with the increase of tensile strain, there is almost no obvious increase in the normalized acoustic nonlinearity (NAN), although this NAN is around two times higher than that of material in elastic deformation. Hong et al. [46] claim the acoustic nonlinearity parameter grows with the propagation distance, which corresponds with the tendency of results showed in Figure 9. Jhang et al. [59,60] performed the acoustic nonlinearity testing on samples with different stresses. The results show that the acoustic nonlinearity increase with the tensile load, which is also consistent with Figure 10. To summarize, the simulation result is reasonable.

5. Conclusions

This investigation demonstrates that MLPGEM can be used to simulate and evaluate plasticity driven material damage based on nonlinear S_0 mode Lamb waves in metallic plates. Simulated results are in accordance with previous theoretical analysis and experimental research for bulk waves or higher-order modes of Lamb waves as primary mode. The results also show that nonlinear Lamb waves based on S_0 mode can be used to assess plasticity driven material damage, or at least monitor the occurrence of plasticity. Further research could develop MLPGEM models with micro-cracks (micro-breathing cracks), dislocations, thermal fatigue, voids, and impurity defects.

Acknowledgments: This work was supported by the National Science Foundation of China (11372104, 11632004, 11604033 and 11602040), and the Key Program for International Science and Technology Cooperation Projects of Ministry of Science and Technology of China (No. 2016YFE0125900).

Author Contributions: N.H., X.L., Y.L., J.Z. and S.F. conceived and designed the simulations; X.S., X.D. and S.Q. performed the simulations; X.S., Y.Z. and J. Z. analyzed the data; N.H. contributed analysis tools; N.H., X.L., Y.L. and F.L. revised the paper; X.S. wrote the paper.

Conflicts of Interest: The authors declare no conflict of interest.

References

1. Rose, J.L. *Ultrasonic Waves in Solid Media*; Cambridge University Press: Cambridge, UK, 1999.
2. Rose, J.L. A baseline and vision of ultrasonic guided wave inspection potential. *J. Press. Vessel Technol.* **2002**, *124*, 273–282. [CrossRef]
3. Raghavan, A.C.; Cesnik, C.E.S. Review of guided-wave structural health monitoring. *Shock Vibr. Dig.* **2007**, *39*, 91–114. [CrossRef]

4. Liu, Y.; Li, Y.; Liu, F.; Morii, M.; Hu, N.; Ning, H.M.; Wu, L.K. Monitoring of local plasticity using Lamb waves. *Adv. Struct. Mater. Eng.* **2015**, *18*, 339–352. [CrossRef]
5. Herrmann, J.; Kim, J.Y.; Jacobs, L.J.; Qu, J.; Littles, J.W.; Savage, M.F. Assessment of material damage in a nickel-base superalloy using nonlinear Rayleigh surface waves. *J. Appl. Phys.* **2006**, *99*, 124913. [CrossRef]
6. Sagar, S.P.; Das, S.; Parida, N.; Bhattacharya, D.K. Non-linear ultrasonic technique to assess fatigue damage in structural steel. *Scr. Mater.* **2006**, *55*, 199–202.
7. Wan, X.; Tse, P.W.; Xu, G.H.; Tao, T.F.; Zhang, Q. Analytical and numerical studies of approximate phase velocity matching based nonlinear S_0 mode Lamb waves for the detection of evenly distributed microstructural changes. *Smart Mater. Struct.* **2016**, *25*, 045023. [CrossRef]
8. Breazeale, M.A.; Thompson, D.O. Finite amplitude ultrasonic waves in aluminum. *Appl. Phys. Lett.* **1963**, *3*, 77–78. [CrossRef]
9. Kim, J.Y.; Jacobs, L.J.; Qu, J.; Littles, J.W. Experimental characterization of fatigue damage in a nickel-base superalloy using nonlinear ultrasonic waves. *J. Acoust. Soc. Am.* **2006**, *120*, 1266–1273. [CrossRef]
10. Matlack, K.H.; Wall, J.J.; Kim, J.Y.; Qu, J.; Jacobs, L.J.; Viehrig, H.W. Evaluation of radiation damage using nonlinear ultrasound. *J. Appl. Phys.* **2012**, *111*, 054911. [CrossRef]
11. Hurley, D.C.; Balzar, D.; Purtscher, P.T. Nonlinear ultrasonic assessment of precipitation hardening in ASTM A710 steel. *J. Mater. Res.* **2000**, *15*, 2036–2042. [CrossRef]
12. Metya, A.; Ghosh, M.; Parida, N.; Sagar, S.P. Higher harmonic analysis of ultrasonic signal for ageing behaviour study of C-250 grade maraging steel. *NDT E Int.* **2008**, *41*, 484–489. [CrossRef]
13. Xiang, Y.; Deng, M.; Xuan, F.Z. Creep damage characterization using nonlinear ultrasonic guided wave method: A mesoscale model. *J. Appl. Phys.* **2014**, *115*, 044914. [CrossRef]
14. Hikata, I.A.; Elbaum, C. Generation of ultrasonic second and third harmonics due to dislocations. *Phys. Rev.* **1966**, *144*, 469–477. [CrossRef]
15. Cantrell, J.H.; Yost, W.T. Acoustic harmonic generation from fatigue-induced dislocation dipoles. *Philos. Mag. A* **1994**, *69*, 315–326. [CrossRef]
16. Cash, W.D.; Cai, W. Dislocation contribution to acoustic nonlinearity: The effect of orientation-dependent line energy. *J. Appl. Phys.* **2011**, *109*, 014915. [CrossRef]
17. Cantrell, J.H. Substructural organization, dislocation plasticity and harmonic generation in cyclically stressed wavy slip metals. *Proc. R. Soc. Lond. A* **2004**, *460*, 757–780. [CrossRef]
18. Cantrell, J.H.; Yost, W.T. Determination of precipitate nucleation and growth rates from ultrasonic harmonic generation. *Appl. Phys. Lett.* **2000**, *77*, 1952–1954. [CrossRef]
19. Yost, W.T.; Cantrell, J.H., Jr.; Breazeale, M.A. Ultrasonic nonlinearity parameters and third-order elastic constants of copper between 300 and 3 °K. *J. Appl. Phys.* **1981**, *52*, 126–128. [CrossRef]
20. Buck, O.; Morris, W.L.; James, M.R. Remaining fatigue life prediction in the initiation regime using SAW NDE. *J. Nondestruct. Eval.* **1980**, *1*, 3–9. [CrossRef]
21. Bermes, C.; Kim, J.Y.; Qu, J.; Jacobs, L.J. Experimental characterization of material nonlinearity using Lamb waves. *Appl. Phys. Lett.* **2007**, *90*, 021901. [CrossRef]
22. De Lima, W.J.N.; Hamilton, M.F. Finite-amplitude waves in isotropic elastic plates. *J. Sound Vib.* **2003**, *265*, 819–839. [CrossRef]
23. Deng, M. Cumulative second-harmonic generation of Lamb-mode propagation in a solid plate. *J. Appl. Phys.* **1999**, *85*, 3051–3058. [CrossRef]
24. Deng, M. Analysis of second-harmonic generation of Lamb modes using a modal analysis approach. *J. Appl. Phys.* **2003**, *94*, 4152–4159. [CrossRef]
25. Deng, M.; Wang, P.; Lv, X. Experimental observation of cumulative second-harmonic generation of Lamb wave propagation in an elastic plate. *J. Phys. D Appl. Phys.* **2005**, *38*, 344–353. [CrossRef]
26. Srivastava, A.; di Scalea, F.L. On the existence of antisymmetric or symmetric Lamb waves at nonlinear higher harmonics. *J. Sound Vib.* **2009**, *323*, 932–943. [CrossRef]
27. Liu, Y.; Chillara, V.K.; Lissenden, C.J. On selection of primary modes for generation of strong internally resonant second harmonics in plate. *J. Sound Vib.* **2013**, *332*, 4517–4528. [CrossRef]
28. Pruell, C.; Kim, J.Y.; Qu, J.; Jacobs, L.J. A nonlinear-guided wave technique for evaluating plasticity-driven material damage in a metal plate. *NDT E Int.* **2009**, *42*, 199–203. [CrossRef]
29. Bermes, C.; Kim, J.Y.; Qu, J.; Jacobs, L.J. Nonlinear Lamb waves for the detection of material nonlinearity. *Mech. Syst. Signal Process.* **2008**, *22*, 638–646. [CrossRef]

30. Li, W.; Cho, Y.; Achenbach, J.D. Detection of thermal fatigue in composites by second harmonic Lamb waves. *Smart Mater. Struct.* **2012**, *21*, 85–93. [CrossRef]
31. Pruell, C.; Kim, J.Y.; Qu, J.; Jacobs, L.J. Evaluation of fatigue damage using nonlinear guide waves. *Smart Mater. Struct.* **2009**, *18*, 035003. [CrossRef]
32. Nucera, C.; di Scalea, F.L. Monitoring load levels in multi-wire strands by nonlinear ultrasonic waves. *Struct. Health Monit.* **2011**, *10*, 617–629. [CrossRef]
33. Zuo, P.; Zhou, Y.; Fan, Z. Numerical and experimental investigation of nonlinear ultrasonic Lamb waves at low frequency. *Appl. Phys. Lett.* **2016**, *109*, 021902. [CrossRef]
34. Chillara, V.K.; Lissenden, C.J. Review of nonlinear ultrasonic guided wave nondestructive evaluation: Theory, numerics, and experiments. *Opt. Eng.* **2016**, *55*, 011002. [CrossRef]
35. Matsuda, N.; Biwa, S. Frequency dependence of second-harmonic generation in Lamb waves. *J. Nondestruct. Eval.* **2014**, *33*, 169–177. [CrossRef]
36. Shan, S.; Cheng, L.; Li, P. Adhesive nonlinearity in Lamb-wave-based structural health monitoring systems. *Smart Mater. Struct.* **2016**, *26*, 025019. [CrossRef]
37. Broda, D.; Staszewski, W.J.; Martowicz, A.; Uhl, T.; Silberschmidt, V.V. Modelling of nonlinear crack–wave interactions for damage detection based on ultrasound—A review. *J. Sound Vib.* **2014**, *333*, 1097–1118. [CrossRef]
38. Wan, X.; Zhang, Q.; Xu, G.; Tse, P.W. Numerical simulation of nonlinear Lamb waves used in a thin plate for detecting buried micro-cracks. *Sensors* **2014**, *14*, 8528–8546. [CrossRef] [PubMed]
39. Shen, Y.; Giurgiutiu, V. Predictive modelling of nonlinear wave propagation for structural healthmonitoring with piezoelectric wafer active sensors. *J. Intell. Mater. Syst. Struct.* **2014**, *25*, 506–520. [CrossRef]
40. Shen, Y.; Cesnik, C.E.S. Modelling of nonlinear interactions between guided waves and fatigue cracks suing local interaction simulation approach. *Ultrasonics* **2017**, *74*, 106–123. [CrossRef] [PubMed]
41. Soleimanpour, R.; Ng, C.T.; Wang, C.H. Higher harmonic generation of guided waves at delaminations in laminated composite beams. *Struct. Health Monit.* **2016**. [CrossRef]
42. Soleimanpour, R.; Ng, C.T. Locating delaminations in laminated composite beams using nonlinear guided waves. *Eng. Struct.* **2017**, *131*, 207–219. [CrossRef]
43. Dziedziech, K.; Pieczonka, L.; Kijanko, P.; Staszewski, W.J. Enhanced nonlinear crack-wave interactions for structural damage detection based on guided ultrasonic waves. *Struct. Control Health Monit.* **2016**, *23*, 1108–1120. [CrossRef]
44. Zhao, Y.X.; Li, F.L.; Cao, P.; Hu, N. Generation mechanism of nonlinear ultrasonic Lamb waves in thin plates with randomly distributed micro-cracks. *Ultrasonics* **2017**, *79*, 60–67. [CrossRef] [PubMed]
45. Rauter, N.; Lammering, R. Numerical simulation of elastic wave propagation in isotropic media considering material and geometrical nonlinearities. *Smart Mater. Struct.* **2015**, *24*, 045027. [CrossRef]
46. Hong, M.; Su, Z.; Wang, Q.; Cheng, L.; Qing, X. Modeling nonlinearities of ultrasonic waves for fatigue damage characterization: Theory, simulation, and experimental validation. *Ultrasonics* **2014**, *54*, 770–778. [CrossRef] [PubMed]
47. Liu, K.; Liu, W. Application of discrete element method for continuum dynamic problems. *Arch. Appl. Mech.* **2006**, *76*, 229–243. [CrossRef]
48. Matlack, K.H.; Kim, J.Y.; Jacobs, L.J.; Qu, J. Experimental characterization of efficient second harmonic generation of Lamb wave modes in a nonlinear elastic isotropic plate. *J. Appl. Phys.* **2011**, *109*, 014905. [CrossRef]
49. Deng, M.; Wang, P.; Lv, X. Experimental verification of cumulative growth effect of second harmonics of Lamb wave propagation in an elastic plate. *Appl. Phys. Lett.* **2005**, *86*, 124104. [CrossRef]
50. Shui, G.; Wang, Y.-S.; Gong, F. Evaluation of plastic damage for metallic materials under tensile load using nonlinear longitudinal waves. *NDT E Int.* **2013**, *55*, 1–8. [CrossRef]
51. Xiang, Y.; Deng, M.; Xuan, F.-Z.; Liu, C.-J. Experimental study of thermal degradation in ferritic Cr–Ni alloy steel plates using nonlinear Lamb waves. *NDT E Int.* **2011**, *44*, 768–774. [CrossRef]
52. Cantrell, J.H. Quantitative assessment of fatigue damage accumulation in wavy slip metals from acoustic harmonic generation. *Philos. Mag.* **2006**, *86*, 1539–1554. [CrossRef]
53. Han, Z.D.; Atluri, S.N. On the (Meshless Local Petrov-Galerkin) MLPG-Eshelby Method in computational finite deformation solid mechanics—Part II. *Comput. Model. Eng. Sci.* **2014**, *97*, 199–237.

54. Atluri, S.N.; Kim, H.G.; Cho, J.Y. A critical assessment of the truly meshless local Petrov-Galerkin (MLPG), and local boundary integral equation (LBIE) methods. *Comput. Mech.* **1999**, *24*, 348–372. [CrossRef]
55. Han, Z.D.; Atluri, S.N. Eshelby stress tensor T: A variety of conservation laws for T in finite deformation anisotropic hyperelastic solid & defect mechanics, and the MLPG-eshelby method in computational finite deformation solid mechanics-part I. *CMES Comput. Model. Eng. Sci.* **2014**, *97*, 1–34.
56. Jensen, A.; Fraser, K.; Laird, G. Improving the precision of discrete element simulations through calibration models. In Proceedings of the 13th International LS-DYNA Conference, Dearborn, MI, USA, 8–10 June 2014.
57. Karajan, N.; Han, Z.D.; Teng, H.; Wang, J. On the parameter estimation for the discrete-element method in LS-DYNA®. In Proceedings of the 13th International LS_DYNA Users Conference, Dearborn, MI, USA, 8–10 June 2014.
58. Yost, W.T.; Cantrell, J.H. The effects of fatigue on acoustic nonlinearity in aluminum alloys. In Proceedings of the 1992 IEEE Ultrasonics Symposium, Tucson, AZ, USA, 20–23 October 1992; Volume 2, pp. 947–955.
59. Jhang, K.Y. Evaluation of material degradation using nonlinear acoustic effect. *Ultrasonics* **1999**, *37*, 39–44. [CrossRef]
60. Jhang, K.Y.; Kim, K.C. Application of nonlinear ultrasonics to the NDE of material degradation. *IEEE Trans. Ultrason. Ferroelectr. Freq. Control* **2000**, *47*, 540–548. [CrossRef] [PubMed]